Impact of Mesh Resolution on Thermo-Mechanical Simulations in Underground Mining Environments: A Comparative Analysis of Field Transfer Methods

Ali AHMADI[1], Michael MARTIN[2] (0009-0003-7881-6456), Eleni GEROLYMATOU[3] (0000-0003-1279-6870) & Jens-André PAFFENHOLZ[4] (0000-0003-1222-5568)

[1] Clausthal University of Technology, ali.ahmadi@tu-clausthal.de
[2] Clausthal University of Technology, michael.dieter.martin@tu-clausthal.de
[3] Clausthal University of Technology, eleni.gerolymatou@tu-clausthal.de
[4] Clausthal University of Technology, jens-andre.paffenholz@tu-clausthal.de (corresponding Author)

DOI: 10.3217/978-3-99161-070-0-012, CC BY 4.0

1 Abstract

Accurate finite element simulations of underground excavations require careful mesh resolution selection, yet systematic methodologies for quantifying mesh-dependent errors in field transfer operations remain underdeveloped. We present a framework for evaluating field transfer accuracy across non-matching meshes in thermo-mechanical simulations, demonstrated through an underground mining drift case study using point clouds from a Zoller+Fröhlich (Z+F) FlexScan 22 mobile mapping system. This work is part of the MOVIE project using the "Reiche Zeche" research and education mine as its underground laboratory. Tetrahedral meshes at four resolutions (5 cm, 9 cm, 20 cm, 50 cm) were generated and embedded within a 100 m host rock domain. Coupled thermo-mechanical simulations were performed in FEniCSx with a transient heat source over 1.58 years. Using the 9 cm resolution as reference, three transfer methods were compared: (1) barycentric interpolation, (2) L^2 Galerkin projection, and (3) cell-based scattered data interpolation. Results show field-type dependence: temperature deviations remained below 0.25%; displacement deviations were approximately 3.5%; von Mises stress exhibited the highest sensitivity at approximately 10%. Cell-based interpolation differed from finite element methods by 87.7% for displacement fields.

2 Introduction

Underground excavations present unique challenges for numerical simulation due to geometric complexity. With the proliferation of laser scanning and mobile mapping technologies, high-resolution point clouds have become standard input for generating computational meshes. However, translating point cloud data to volumetric meshes introduces fundamental decisions regarding mesh resolution that propagate through all subsequent analyses.

The generation of finite element meshes from point cloud data has received considerable attention. ZHANG et al. (2005) established foundational methods for creating 3D meshes from imaging data, while CASTELLAZZI et al. (2017) developed procedures for converting laser scanning data into finite element models. CASTELLAZZI et al. (2022) introduced Cloud2FEM for existing structures. Mesh resolution significantly impacts accuracy, with CAO et al. (2023) demonstrating errors varying by orders of magnitude, while MOREIRA et al. (2022) proposed adaptive refinement strategies.

When transferring field data between non-matching meshes, methodology choice significantly impacts quality. FARRELL and MADDISON (2011) developed conservative interpolation schemes, demonstrating that naÃ¯ve approaches introduce spurious oscillations. BUSSETTA et al. (2012) proposed efficient 3D transfer operators, and REBEROL and LÉVY (2018) developed GPU-accelerated methods for disparate meshes.

This paper addresses the gap in systematic frameworks for underground excavation modelling through a case study within the MOVIE project, using the "Reiche Zeche" research and education mine. Using point cloud data from a Zoller+Fröhlich (Z+F) FlexScan 22 mobile mapping platform, we generated tetrahedral meshes at four resolutions: 5 cm, 9 cm, 20 cm, and 50 cm. Taking the 9 cm mesh as reference, three field transfer methodologies were evaluated:

1. **Barycentric interpolation** (BARATTA et al., 2023): Direct interpolation within FEniCSx.
2. L^2 **Galerkin projection** (BOCHEV and SHASHKOV, 2005): Variational approach minimising the L^2 norm difference.
3. **Cell-based scattered data interpolation** (SCHROEDER et al., 2006): Point-location approach via VTK.

Error quantification employed discrete L^2 norms. Additionally, structured-grid round-trip analyses isolated intrinsic interpolation errors from mesh-dependent solution differences. Section 3 details the methodology; Section 4 presents results; Section 5 interprets findings; Section 6 summarises conclusions.

3 Methodology

3.1 Study Site and Data Acquisition

The study site is the "Reiche Zeche" research and education mine in Freiberg, Germany, operated by TU Bergakademie Freiberg since 1919, with underground drifts extending over 19 km at depths up to 230 m. The region of interest at "Sohle 1" (147 m depth) comprises a drift system with irregular wall surfaces typical of historical mining excavations (MISCHO, 2014).

Point cloud data were acquired using a Z+F FlexScan 22 mobile mapping platform (Figure 1), operating as an extension unit on the Z+F IMAGER 5016A laser scanner with SLAM capability. The system provides 360° horizontal and 320° vertical field of view with measurement ranges

from 0.3 m to 365 m.

Abb. 1: Z+F FlexScan 22 mobile mapping platform with IMAGER 5016A laser scanner.

Two overlapping point clouds were processed in Z+F LaserControl through preprocessing, trajectory optimisation, and 3D filtering. Registration used the ICP algorithm (BESL and MCKAY, 1992):

$$E(\boldsymbol{R},\boldsymbol{t}) = \sum_{i=1}^{N} \|\boldsymbol{R}\boldsymbol{p}_i + \boldsymbol{t} - \boldsymbol{q}_i\|^2 \tag{1}$$

The combined cloud was subsampled to 1 cm resolution and surface normals were computed using a quadric local surface model. Figure 2 presents the point cloud with Chamber 1 highlighted, which contains the fictitious heat source location and serves as the primary visualisation region throughout this study.

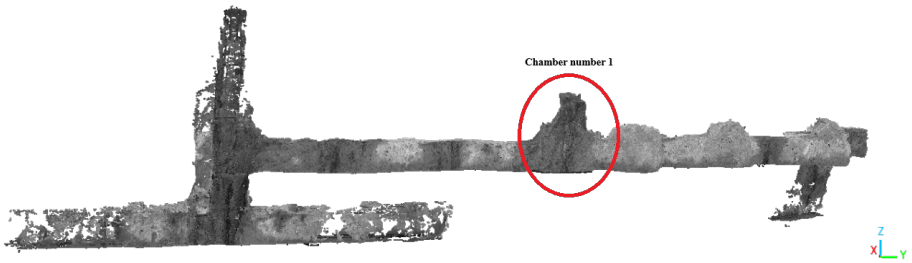

(a) Complete drift network with Chamber 1 indicated

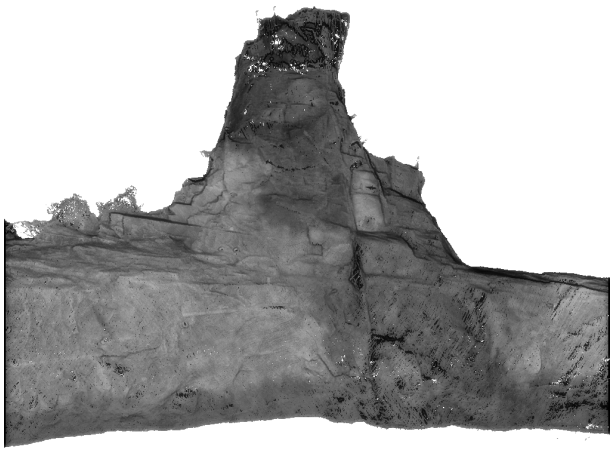

(b) Chamber 1 detail (animated)

Abb. 2: Raw point cloud after registration: (a) overview showing the complete tunnel system with Chamber 1 circled; (b) animated visualisation zooming into Chamber 1 to illustrate point cloud resolution and surface detail.

3.2 Mesh Generation

3.2.1 Surface Reconstruction

Surface mesh generation used Screened Poisson Surface Reconstruction (KAZHDAN and HOPPE, 2013) in MeshLab. Given oriented points $\mathscr{P} = \{(\boldsymbol{p}_i, \boldsymbol{n}_i)\}$, the algorithm constructs an indicator function χ satisfying:

$$\Delta\chi - \alpha\chi = \nabla \cdot \boldsymbol{V} \tag{2}$$

Following reconstruction with octree depth 10, isotropic remeshing achieved uniform edge lengths at four resolutions: 5 cm, 9 cm, 20 cm, and 50 cm. A structured hexahedral mesh was also generated for round-trip error analysis. Figure 3 presents the surface meshes.

3.2.2 Volumetric Meshing

Volumetric meshing was performed in GMSH (GEUZAINE and REMACLE, 2009) by embedding each surface mesh within a cuboidal host rock domain expanded by 100 m. The volume was discretised using constrained Delaunay tetrahedralisation with Netgen optimisation

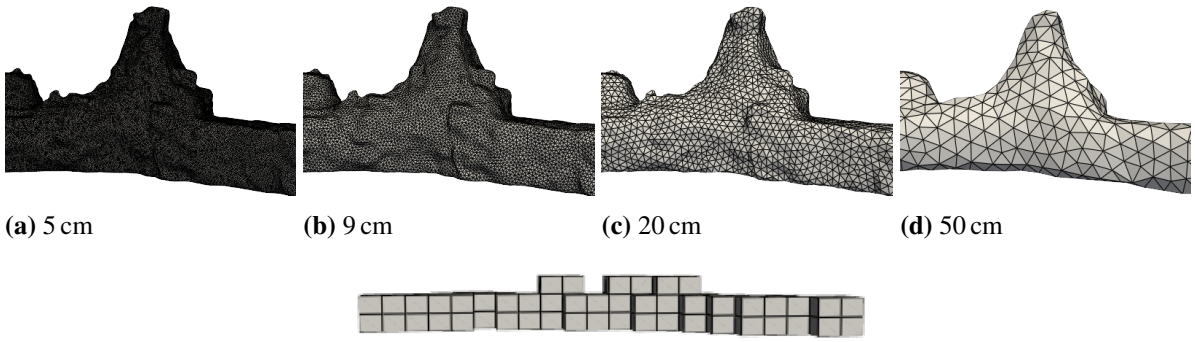

(a) 5 cm **(b)** 9 cm **(c)** 20 cm **(d)** 50 cm

(e) Structured hexahedral grid

Abb. 3: Surface meshes at Chamber 1: (a)–(d) triangular meshes at four resolutions showing progressive geometric simplification from fine (5 cm) to coarse (50 cm); (e) structured hexahedral mesh used exclusively for round-trip transfer error evaluation—note this is a geometrically distinct mesh with regular hexahedral elements, not a coarser variant of the triangular meshes.

(SCHÖBERL, 1997). Table 1 summarises mesh characteristics.

Tabelle 1: Volumetric mesh statistics for the four surface resolutions.

Resolution	Nodes	Elements	Element Type
5 cm	296,019	1,471,842	Tetrahedral
9 cm	75,171	379,254	Tetrahedral
20 cm	20,307	103,489	Tetrahedral
50 cm	3,664	19,320	Tetrahedral

3.3 Thermo-Mechanical Simulation

Monolithic thermo-mechanical simulations were performed in FENICSX (BARATTA et al., 2023). The coupled formulation solves for temperature T and displacement $\boldsymbol{u}$ simultaneously using first-order Lagrange (CG1) elements for both fields. First-order elements were used for both fields instead of an optimal Taylor-Hood formulation to reduce simulation time. Figure 4 presents the Newton-Raphson algorithm and governing equations.

The linearised system is solved using GMRES (SAAD and SCHULTZ, 1986) with Boomer-AMG preconditioning (HENSON and YANG, 2002). Time integration uses backward Euler with $\Delta t = 5 \times 10^7$ s (1.58 years) over two steps. Figure 6 shows the 9 cm volumetric mesh.

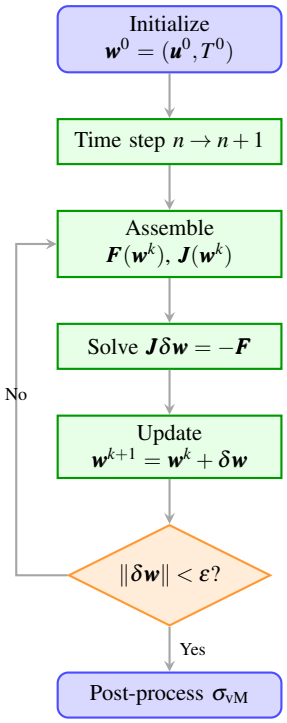

Governing equations:

$$\rho c \frac{\partial T}{\partial t} = \nabla \cdot (\kappa \nabla T) \tag{3}$$

$$\nabla \cdot \boldsymbol{\sigma} + \rho \boldsymbol{g} = \boldsymbol{0} \tag{4}$$

Constitutive relations:

$$\boldsymbol{\sigma} = \boldsymbol{C} : (\boldsymbol{\varepsilon} - \boldsymbol{\varepsilon}_{\mathrm{th}}) \tag{5}$$

$$\boldsymbol{\varepsilon}_{\mathrm{th}} = \alpha_{\mathrm{th}} (T - T_0) \boldsymbol{I} \tag{6}$$

Weak form residual:

$$\boldsymbol{F}(\boldsymbol{w}) = \boldsymbol{F}_{\mathrm{mech}} + \boldsymbol{F}_{\mathrm{therm}} = \boldsymbol{0} \tag{7}$$

where thermal and mechanical parts are coupled through thermal strain $\boldsymbol{\varepsilon}_{\mathrm{th}}$.

Abb. 4: Left: Newton-Raphson solution algorithm flowchart. Right: Governing equations and constitutive relations for coupled thermo-mechanical analysis.

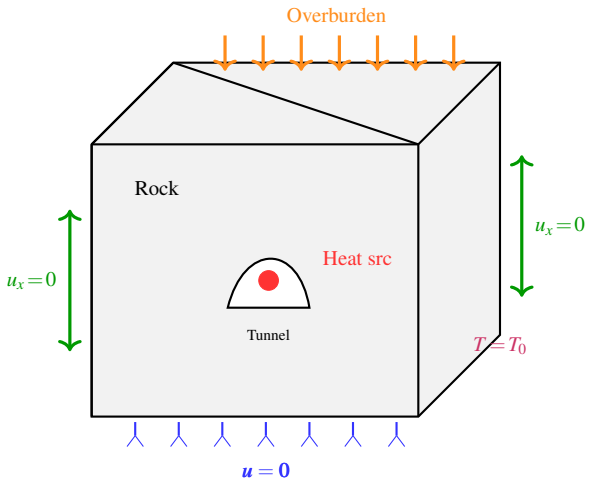

Abb. 5: Boundary conditions schematic.

BCs: fixed ($\boldsymbol{u} = \boldsymbol{0}$) bottom; roller on sides; 30 m overburden top; $T_0 = 10\,^{\circ}\mathrm{C}$ outer faces.
Heat source: $T_f = 300\,^{\circ}\mathrm{C}$ fictitious sphere ($R = 0.2\,\mathrm{m}$) at $(12, -15, -159)$ m.

Tabelle 2: Material properties (gneiss).

Parameter	Value
κ (thermal conductivity)	$3.0\,\mathrm{W/(m \cdot K)}$
ρ (density)	$2700\,\mathrm{kg/m^3}$
c (specific heat)	$1060\,\mathrm{J/(kg \cdot K)}$
E (Young's modulus)	50 GPa
ν (Poisson's ratio)	0.25
α_{th} (thermal expansion)	$8 \times 10^{-6}/\mathrm{K}$

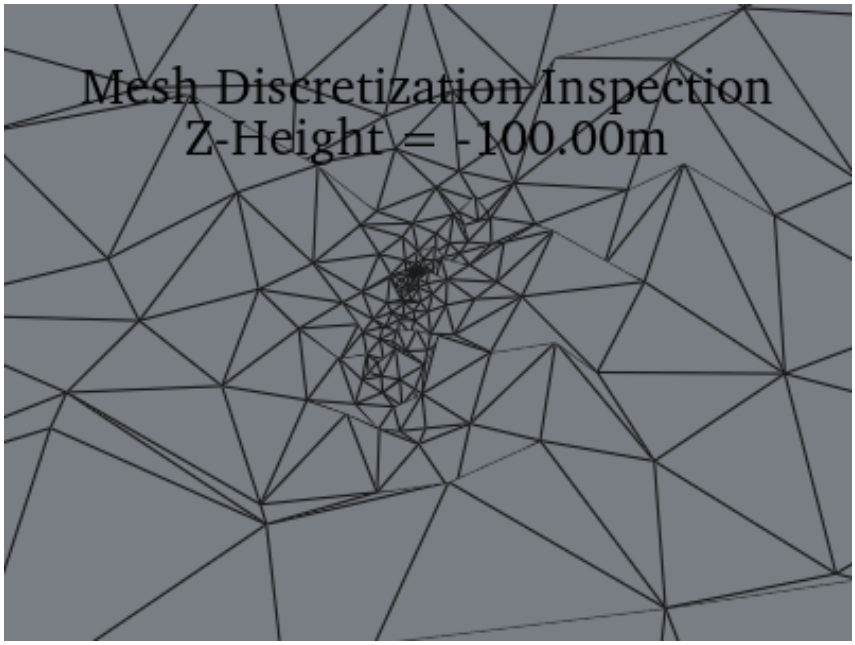

Abb. 6: Volumetric mesh at 9 cm resolution (animated) showing tunnel embedded in host rock domain.

3.4 Field Transfer Methods

Three methodologies were evaluated:

Barycentric Interpolation: For each target node $\boldsymbol{x}_i$, interpolated values use shape functions:

$$f(\boldsymbol{x}_i) = \sum_{j=1}^{n} N_j(\boldsymbol{x}_i)\, f_j \tag{8}$$

Implemented in FEniCSx with coupled vector treatment.

L^2 Galerkin Projection: The projected field minimises the L^2 difference (BOCHEV and SHASHKOV, 2005):

$$\int_\Omega f^{\text{tgt}}\, v \,\mathrm{d}\Omega = \int_\Omega f^{\text{src}}\, v \,\mathrm{d}\Omega \quad \forall v \in V^{\text{tgt}} \tag{9}$$

Cell-Based Interpolation: Via VTK's `vtkProbeFilter` (SCHROEDER et al., 2006) with nearest-neighbour extrapolation, processing vector components independently.

3.5 Error Quantification

Field transfer accuracy used discrete L^2 norms:

$$\|e\|_{L^2} = \left(\int_\Omega |e|^2 \,\mathrm{d}\Omega \right)^{1/2} \tag{10}$$

Relative errors: $\varepsilon_{L^2}^{\text{rel}} = \|e\|_{L^2} / \left\|f^{\text{mapped}}\right\|_{L^2}$. All comparisons used the 9 cm mesh as reference. Round-trip analysis isolated intrinsic interpolation errors from mesh-dependent solution differences.

4 Results

All results use the 9 cm resolution simulation as reference. Selected figures contain embedded animations viewable in Adobe Acrobat Reader or compatible PDF viewers.

4.1 Reference Solution

Figure 7 shows reference results after 1.58 years. The heat source induces localised temperature elevation up to 300 °C with corresponding thermo-mechanical deformation. Displacement reaches millimetre scale; von Mises stress concentrates at tunnel boundaries.

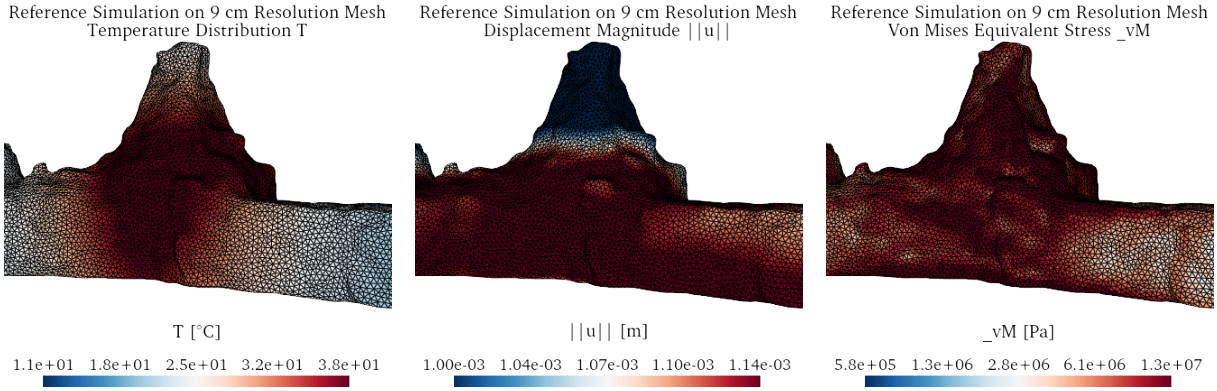

(a) Temperature T (animated) **(b)** Displacement $\|\boldsymbol{u}\|$ **(c)** Von Mises σ_{vM}

Abb. 7: Reference solution on 9 cm mesh showing: (a) temperature distribution with heat diffusion from the spherical source; (b) displacement magnitude indicating thermo-mechanical deformation; (c) von Mises stress distribution with concentrations at tunnel boundary. Red sphere marks heat source location.

4.2 Barycentric Interpolation Deviations

Table 3 and Figure 8 present barycentric interpolation results. Temperature transferred with excellent accuracy (below 0.25%). Displacement showed consistent ≈3.5% deviations dominated by geometric discretisation. Von Mises stress showed highest sensitivity at ≈10.4%.

Tabelle 3: Relative L^2 deviations [%] for barycentric interpolation from 9 cm reference.

Target	Temperature	Displacement	Von Mises
5 cm	0.09	3.61	10.4
20 cm	0.06	3.59	10.3
50 cm	0.25	3.49	10.5

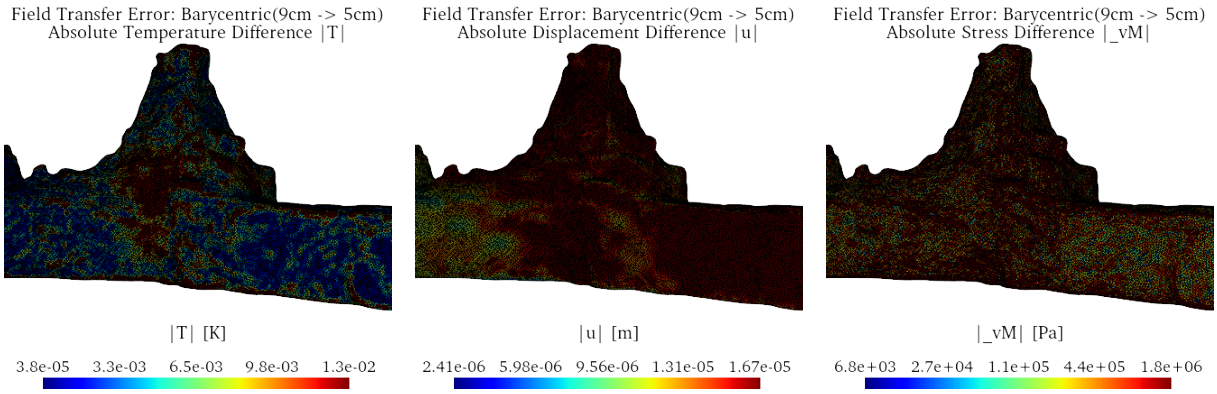

(a) $|\Delta T|$, 5 cm (animated) **(b)** $|\Delta \boldsymbol{u}|$, 5 cm **(c)** $|\Delta \sigma_{\mathrm{vM}}|$, 5 cm

Abb. 8: Barycentric interpolation deviations from 9 cm reference to 5 cm target mesh: (a) temperature difference showing sub-percent deviations; (b) displacement difference concentrated near tunnel boundary; (c) von Mises stress difference showing highest sensitivity.

4.3 L^2 Galerkin Projection Deviations

Table 4 shows L^2 projection results. Temperature and displacement matched barycentric interpolation. Von Mises stress showed degraded accuracy (11.9%–22.9%) because projection smooths discontinuous fields.

Tabelle 4: Relative L^2 deviations [%] for L^2 Galerkin projection from 9 cm reference.

Target	Temperature	Displacement	Von Mises
5 cm	0.09	3.61	11.9
20 cm	0.06	3.59	18.9
50 cm	0.25	3.49	22.9

4.4 Cell-Based Scattered Data Interpolation Deviations

Table 5 shows cell-based interpolation results. Temperature remained below 1%. Displacement deviations appear lower (0.89–1.93%) but reflect component-wise processing. Von Mises stress increased substantially with coarsening (16.5%–24.6%).

Tabelle 5: Relative L^2 deviations [%] for cell-based scattered data interpolation from 9 cm reference.

Target	Temperature	Displacement	Von Mises
5 cm	0.32	0.89	16.5
20 cm	0.37	1.15	16.3
50 cm	0.66	1.93	24.6

4.5 Structured Grid Round-Trip Analysis

Round-trip analysis (reference $\rightarrow$ structured $\rightarrow$ reference $\rightarrow$ structured) isolates intrinsic interpolation errors from mesh-dependent solution differences. Table 6 compares results. Both methods achieved sub-percent deviations for temperature (0.70%) and displacement (0.69%), confirming high intrinsic accuracy. The 0.69% displacement round-trip deviation demonstrates that the larger 3.5% cross-mesh deviations arise from comparing solutions on geometrically different meshes rather than from interpolation limitations. For von Mises stress, barycentric interpolation achieved 0.22% versus 11.95% for L^2 projection—a 54-fold difference demonstrating that variational projection corrupts discontinuous field representations.

Tabelle 6: Relative L^2 deviations [%] for structured grid round-trip analysis.

Method	Temperature	Displacement	Von Mises
Barycentric Interpolation	0.70	0.69	0.22
L^2 Galerkin Projection	0.70	0.69	11.95

4.6 Pairwise Method Comparison

Figure 9 and Table 7 quantify method differences. Finite element methods produced identical results for continuous fields ($< 10^{-9}$%). Cell-based interpolation exhibited 87.7% difference for displacement and 44% for von Mises stress.

Tabelle 7: Pairwise method comparison on structured grid: relative L^2 differences [%].

Comparison	Temp.	Disp.	Von Mises
L^2 Proj. vs Baryc. Interp.	$< 10^{-9}$	$< 10^{-9}$	4.3
L^2 Proj. vs Cell-Based	$< 10^{-4}$	87.7	43.8
Baryc. Interp. vs Cell-Based	$< 10^{-4}$	87.7	44.1

4.7 Summary

Figure 10 compares relative L^2 errors across all fields, resolutions, and methods.

Principal findings: temperature transfers with sub-percent deviations; displacement exhibits 3.5% cross-mesh deviations with 0.69% round-trip accuracy; von Mises stress shows 10–25% deviations with barycentric outperforming L^2 projection by 54$\times$; finite element methods out-

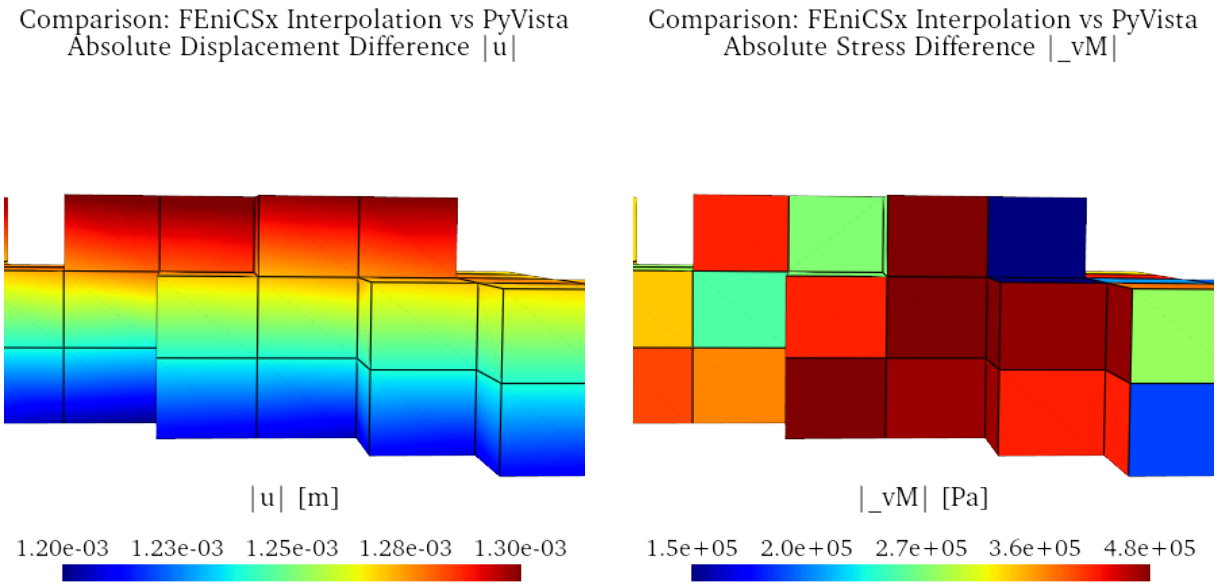

(a) $|\Delta \boldsymbol{u}|$: 87.7% difference (animated) **(b)** $|\Delta \sigma_{\mathrm{vM}}|$: 44.1% difference

Abb. 9: Difference between barycentric interpolation and cell-based scattered data interpolation on the structured hexahedral grid: (a) displacement field showing 87.7% relative difference; (b) von Mises stress showing 44.1% relative difference. These large discrepancies highlight fundamental differences between finite element and general-purpose interpolation approaches.

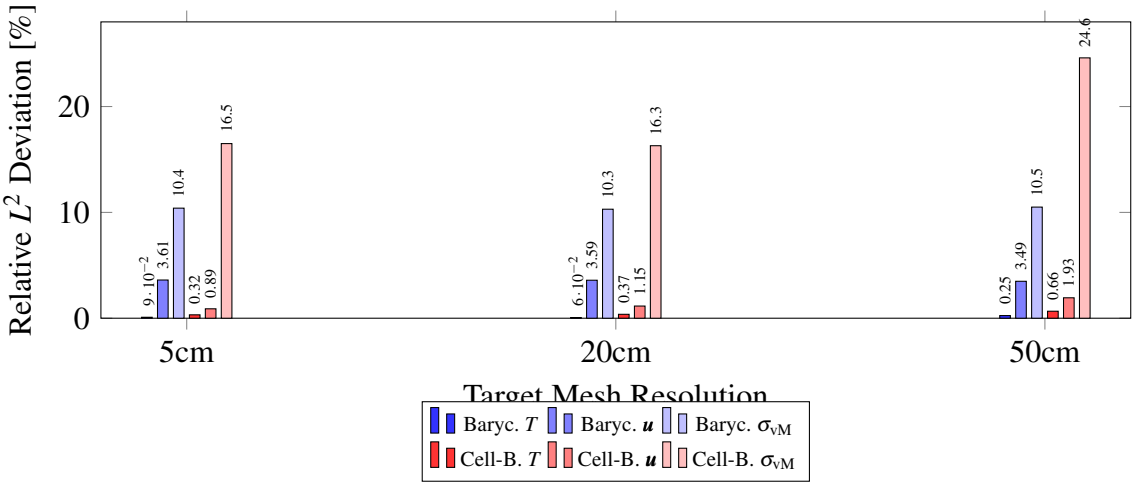

Abb. 10: Comparison of relative L^2 deviations: barycentric interpolation (blue) versus cell-based scattered data interpolation (red) from 9 cm reference to target meshes.

perform cell-based interpolation for vector fields (87.7% difference).

5 Discussion

5.1 Field-Dependent Transfer Accuracy

Temperature's excellent transfer accuracy reflects the smooth, slowly-varying nature of thermal fields, which are well-represented by low-order finite elements regardless of mesh resolution. Displacement's consistent deviations across all target resolutions indicate that differences are dominated by geometric discretisation effects rather than interpolation artefacts, confirmed by sub-percent round-trip deviation. Von Mises stress shows highest sensitivity as a derived quantity computed from displacement gradients; the 54-fold difference between barycentric and L^2 projection demonstrates that variational projection—while optimal for continuous fields—fundamentally corrupts discontinuous field representations.

5.2 Transfer Method Selection

Continuous scalar fields: Both methods provide equivalent accuracy; direct interpolation preferred for lower cost.

Continuous vector fields: Finite element interpolation maintains coupled treatment, outperforming component-wise approaches (87.7% difference).

Discontinuous fields: Direct interpolation substantially outperforms L^2 projection.

5.3 Practical Recommendations

The 9 cm resolution provides practical balance—four-fold element reduction compared to the 5 cm mesh while maintaining sub-percent transfer accuracy for continuous fields. However, establishing absolute solution accuracy would require mesh convergence studies with progressively refined meshes, which was beyond the scope of this field transfer investigation.

For repository safety assessments, temperature field transfer is adequate even with substantial resolution differences. Stress-based safety indicators require careful mesh convergence studies due to inherent discretisation dependence. The substantial difference between finite element and cell-based implementations highlights the importance of consistent tool selection within coupled simulation pipelines—mixing implementations from different libraries may introduce unexpected discrepancies.

6 Conclusion

This study presented a framework for evaluating field transfer accuracy across non-matching meshes in thermo-mechanical simulations. Using point cloud data from the "Reiche Zeche" research mine, we compared three transfer methodologies across four mesh resolutions.

Principal findings:

1. **Temperature fields** transfer with high accuracy ($< 0.25\%$ deviation).
2. **Displacement fields** exhibit $\approx 3.5\%$ transfer deviations with 0.69% round-trip accuracy.
3. **Von Mises stress** shows highest sensitivity ($\approx 10\%$ deviation).
4. **Method selection critically affects discontinuous fields**: Barycentric outperforms L^2 projection by $54\times$.
5. **Implementation matters**: Cell-based differs from finite element by 87.7% for displacement.

The 9 cm resolution was selected as the reference, achieving approximately four-fold element reduction compared to the 5 cm mesh (379,254 vs 1,471,842 elements) while maintaining sub-percent transfer accuracy for continuous fields. The framework offers evidence-based guidance for transfer method selection in point cloud based underground models, contributing to the MOVIE project's virtual laboratory development.

Acknowledgments

The project "MOdellkopplung im Kontext eines VIrtuellen Untertagelabors und dessen Entwicklungsprozess – MOVIE" is part of the research program "GEO:N - Geosciences for Sustainability" on the topic "Digital Geosystems: Virtual Methods and Digital Tools for Geoscientific Applications" funded by the German Federal Ministry of Research, Technology and Space (BMFTR). GEO:N is thus part of the BMFTR program "Research for Sustainable Development (FONA)". For the opportunity to realize this project, the consortium thanks the BMFTR and the project management organization. [Reference: 03G0921A / 2024-01 till 2026-12]

References

BARATTA, I. A., DEAN, J. P., DOKKEN, J. S., HABERA, M., HALE, J. S., RICHARDSON, C. N., ROGNES, M. E., SCROGGS, M. W., SIME, N., and WELLS, G. N., (2023): DOLFINx: The next generation FEniCS problem solving environment. In: *Zenodo*. 10.5281/zenodo.10447666.

BESL, P. J. and MCKAY, N. D., (1992): A method for registration of 3-D shapes. In: *IEEE Transactions on Pattern Analysis and Machine Intelligence*, 14(2), 239–256. 10.1109/34.121791.

BOCHEV, P. and SHASHKOV, M., (2005): Constrained interpolation (remap) of divergence-free fields. In: *Computer Methods in Applied Mechanics and Engineering*, 194(2–5), 511–530. 10.1016/j.cma.2004.01.027.

BUSSETTA, P., MARCEAU, D., and PONTHOT, J.-P., (2012): The adapted augmented Lagrangian method: a new method for the resolution of the mechanical frictional contact problem. In: *Computational Mechanics*, 49(2), 259–275. 10.1007/s00466-011-0644-z.

CAO, Y. et al., (2023): The relationship between mesh resolution and accuracy for finite element simulations. In: *Computational Mechanics*, 71, 1–15.

CASTELLAZZI, G., D'ALTRI, A. M., DE MIRANDA, S., and UBERTINI, F., (2017): An innovative numerical modeling strategy for the structural analysis of historical monumental buildings. In: *Engineering Structures*, 132, 229–248. 10.1016/j.engstruct.2016.11.032.

CASTELLAZZI, G., D'ALTRI, A. M., DE MIRANDA, S., CHIOZZI, A., and TRALLI, A., (2022): Cloud2FEM: A finite element mesh generator based on point clouds of existing/historical structures. In: *SoftwareX*, 18, 101099. 10.1016/j.softx.2022.101099.

FARRELL, P. E. and MADDISON, J. R., (2011): Conservative interpolation between volume meshes by local Galerkin projection. In: *Computer Methods in Applied Mechanics and Engineering*, 200(1–4), 89–100. 10.1016/j.cma.2010.07.015.

GEUZAINE, C. and REMACLE, J.-F., (2009): Gmsh: A 3-D finite element mesh generator with built-in pre- and post-processing facilities. In: *International Journal for Numerical Methods in Engineering*, 79(11), 1309–1331. 10.1002/nme.2579.

HENSON, V. E. and YANG, U. M., (2002): BoomerAMG: A parallel algebraic multigrid solver and preconditioner. In: *Applied Numerical Mathematics*, 41(1), 155–177. 10.1016/S0168-9274(01)00115-5.

KAZHDAN, M. and HOPPE, H., (2013): Screened Poisson surface reconstruction. In: *ACM Transactions on Graphics*, 32(3), 29:1–29:13. 10.1145/2487228.2487237.

MISCHO, H., (2014): Der Ausbau des Forschungs- und Lehrbergwerks der TU Bergakademie Freiberg zum zentralen Forschungsstandort unter Tage. In: *15. Geokinematischer Tag*, 1–18, Freiberg, Germany, TU Bergakademie Freiberg.

MOREIRA, R. et al., (2022): Multi-criteria adaptive mesh refinement for additive manufacturing simulations. In: *Additive Manufacturing*, 52, 102689.

REBEROL, M. and LÉVY, B., (2018): Computing the distance between two finite element solutions defined on different 3d meshes on a GPU. In: *SIAM Journal on Scientific Computing*, 40(1), C131–C155. 10.1137/17M1115976.

SAAD, Y. and SCHULTZ, M. H., (1986): GMRES: A generalized minimal residual algorithm for solving nonsymmetric linear systems. In: *SIAM Journal on Scientific and Statistical Computing*, 7(3), 856–869. 10.1137/0907058.

SCHÖBERL, J., (1997): NETGEN an advancing front 2D/3D-mesh generator based on abstract rules. In: *Computing and Visualization in Science*, Vol. 1, 41–52. 10.1007/s007910050004.

SCHROEDER, W., MARTIN, K., and LORENSEN, B., (2006): *The Visualization Toolkit: An Object-Oriented Approach to 3D Graphics*. 4th edn., Kitware.

ZHANG, Y., BAJAJ, C., and SOHN, B.-S., (2005): 3d finite element meshing from imaging data. In: *Computer Methods in Applied Mechanics and Engineering*, 194(48–49), 5083–5106. 10.1016/j.cma.2004.11.026.